Drag analysis with a self-propelled flexible swimmer

David Gross [1], Yann Roux,[1] Christophe Raufaste [2,3] and Médéric Argentina [2,*]

[1]*MyCFD S.A.S., 1300 Route des Cretes, 06560 Valbonne, France*

[2]*Université Côte d'Azur, CNRS, INPHYNI, 06100 Nice, France*

[3]*Institut Universitaire de France (IUF), Paris, France*

(Received 28 October 2020; accepted 29 March 2021; published 3 May 2021)

Fish swim by undulating their body to ensure propulsion. In steady state, thrust is balanced by a total drag force, whose dominant terms depend on the Reynolds number and on the flow regime. If skin friction prevails on pressure drag in the laminar regime, and conversely in the turbulent regime, it is not clear how important is the contribution of the vortex-induced drag in both regimes. In this article, we tackle both flow regimes within the same numerical framework to address this question and the relevant scaling laws at play. In particular, we show in the turbulent regime that the combination of both the pressure and vortex-induced drags sets the Strouhal number between 0.2 and 0.4 following the thrust and drag balance, in very good agreement with natural swimmers. In the laminar regime, the vortex-induced drag can be neglected in most cases. If not, we rationalize the correction and show that our two-dimensional swimmer needs to account for a significant amplification of the drag force to match the biological data.

DOI: 10.1103/PhysRevFluids.6.053101

I. INTRODUCTION

Nature provides an intriguing form of propulsion based on traveling undulatory body waves as observed in many fish species [1]. The choice of gait parameters is of interest to understand if fundamental trends can be identified in all swimmers. The work of Bainbridge [2,3] suggested that swimming speed U was proportional to tail beat amplitude A with amplitude increasing with frequency up to a maximum of about $0.2L$. Likewise, he corroborated that the swimming speed was proportional to the tail beat frequency f or angular frequency $\omega = 2\pi f$, for a given body length [2]. Following Bainbridge, Webb and Kostecki [4] also identified a linear relation of tail beat frequency to swimming speed which was found to be proportional to the product of f and Ar [5]. Triantafyllou introduced the use of Strouhal number $\mathrm{St} = fA/U$ to characterize fish swimming [6,7] and he showed that for flapping foils, an optimum in efficiency is observed around a St of 0.25–0.35 [8]. This almost constant Strouhal number hypothesis has been challenged in living animals: tailbeat frequency and amplitude were measured on American eels *Anguilla rostrata* by Tytell [9] who found that the eels always swam with near constant St for a given swimming speed, but varied the amplitude and frequency along isocontours of constant St. More recently, Eloy *et al.* elaborated on Triantafyllou by showing the choice of optimal St was in fact a function of drag coefficient and they established that for increasing drag coefficients, optimal St increased [10]. In this optimization process, they exploited a viscous drag equal to twice that of a laminar or turbulent flat plate.

Actually, the constancy of the Strouhal number around 0.3 [6,11–13] is found in the high Reynolds numbers, or turbulent, regime with typical Re larger than approximately 3000 [12]. This indicates a correlation with the nature of the drag force, dominated by "inertial" drag over skin

*Author to whom correspondence should be addressed

friction. With a balance between a thrust per unit depth scaling as $\rho f^2 A^2 L$ with L the fish length, and a drag per unit depth scaling as $\rho U^2 L$ and $\rho U^2 L/\sqrt{\mathrm{Re}}$ in the turbulent and laminar regimes, respectively [12], simple scaling relations are derived:

$$\begin{aligned} &\mathrm{Re} \propto \mathrm{Sw}^{\frac{4}{3}} \quad \text{or} \quad \mathrm{St} \propto \mathrm{Sw}^{-\frac{1}{4}} \quad \text{for} \quad \mathrm{Re} < 3000, \\ &\mathrm{Re} \propto \mathrm{Sw} \quad \text{or} \quad \mathrm{St} \propto \text{constant} \quad \text{for} \quad \mathrm{Re} > 3000 \end{aligned} \tag{1}$$

with the Reynolds number $\mathrm{Re} = UL/\nu$, the swimming number $\mathrm{Sw} = \omega AL/\nu$, and the kinematic viscosity ν. The swimming number can be interpreted as a Reynolds number based on the transverse velocity of the undulating tail. This rather simplistic approach was successful in predicting the swimming speed over seven orders of magnitude of the Reynolds number [12]. In addition, fish are very efficient swimmers since the values of the Strouhal number in the turbulent regime match what is expected if the propulsive part of the fish works at maximal efficiency [14]. In the same vein and on the example of fishlike artificial swimmers, the constancy of the ratio $A/L = A^\star \sim 0.2$ could be rationalized as the minimum energy expenditure to swim [13]. On the other hand, calculations based on potential flows give ideas of the relevant forces at play associated to the undulations of a swimmer. In the small amplitude regime, we expect the dynamical pressure to be proportional to A at the leading order. As the swimmer's body makes a local angle with the direction of motion that scales as $A^\star$, projecting the force induced by the pressure onto the direction of motion leads to a total force proportional to A^2. Calculations performed with rigid [15] or flexible [16] objects oscillating at small amplitude reveal terms proportional to 1, U and U^2. As a consequence, dimensional analysis leads to longitudinal forces scaling as $\rho L A^2 f^2$, $\rho U A^2 f$, and $\rho U^2 A^2/L$, respectively. The first scaling is propulsive and corresponds to the thrust generated by the added mass accelerated by the swimmer. It has been validated with experimental systems such as heaving foils [17], pitching foils [18], foils combining both of them [14], and flexible robotic fish [19]. The second and third scalings give resistive forces associated to the shedding of vortices in the wake of the swimmer. The term $\rho U A^2 f$ measures the drag induced by the unsteady motion, while the term $\rho U^2 A^2/L$ is related to the equivalent force exerted on an inclined stationary hydrofoil in a steady flow (the so-called lift-induced drag). In addition, we expect terms in A^4 associated to larger amplitudes or three-dimensional (3D) effects [20]. The two contributions of the vortex-induced drag are not accounted for in the relations (1) and we question here the relevance of these two terms, both in the turbulent and laminar regimes. We first consider the turbulent regime. Simple dimensional analysis shows that the Strouhal number depends on $A^\star$ and C_P only [13,19], with C_P the pressure drag coefficient that weights the drag expression. In the small-amplitude regime, experiments with flexible panels or robots show that the Strouhal number is in fact independent of the swimming velocity and of the tail beat frequency [13,17,19], and simple models of locomotion retrieve that the Strouhal number scales as $\sqrt{C_P}$ [21]. By measuring separately the thrust and the pressure drag experimentally with a robotic fish, Gibouin *et al.* [19] noticed that St is constant only for small $A^\star$ and increases as $A^\star$ increases, which is different from what is expected by the simple force balance of Eq. (1). Our hypothesis is that this trend can be associated with the two contributions of the vortex-induced drag. If $A \ll L$ these contributions can be neglected with respect to pressure drag, but this does not hold necessarily as $A \sim L$. In addition, even though values of the pressure drag coefficient C_P are difficult to infer from experiments since they require measurements when fish do not make any movement, data collected either with dead fish or during gliding deceleration for a large variety of species (salmon, herring, and trout [22]; cods [23]; bluegill [24]; dolphins [25,26]; others reviewed by [24]) suggest that this coefficient ranges between 0.003 and 0.1 in the turbulent regime. These values span over several orders of magnitude and are significantly smaller than unity, which opens the question of the relevance of the vortex-induced drag in the final force balance and how it affects the second scaling in Eq. (1). In particular, we will show that accounting for the vortex-induced drag in the force balance sets $\mathrm{St} \simeq 0.3$ for $A^\star \simeq 0.2$ whatever the value of the pressure drag coefficient. This result is in agreement with observations performed with natural swimmers.

In the laminar regime, drag is expected to be dominated by skin friction. Lighthill [22] speculated that the boundary layer of swimmers is thinned by their transverse motions such that an increase in skin friction drag is seen as part of what is referred to as the "Bone-Lighthill boundary layer thinning hypothesis." Ehrenstein and Eloy [27–29] investigated this hypothesis for the laminar flow regime both numerically with a two-dimensional (2D) and 3D direct numerical simulation (DNS) code and analytically: they conclude that the drag increase is proportional to the square root of the perpendicular velocities [27]. Pursuing this further with a 3D boundary layer model and 3D numerical results, they found a 40% increase in skin friction drag analytically and between 70% and 100% greater skin friction numerically [27,28]. It is thus not clear how the enhancement of skin friction, as compared to the one obtained with a regular Blasius boundary layer, affects the first scaling relation in Eq. (1), nor how this component of the total drag force compares to the vortex-induced drag component.

In this article, we exploit numerical simulations to address the questions relative to the various drag at play in undulating swimmers. Using a 2D viscous CFD approach, Carling *et al.* represented an early attempt to perform solved motion, self-propelled swimming with an imposed body deformation [30] which inspired numerous other authors [31,32]. The use of inviscid boundary element (panel) methods has seen widespread use in studying swimming. Pedley and Hill used 2D vortex lattice approach with vortex particles to represent the wake [33]. In the same vein, we use the 2D unsteady panel method described in [34] to simulate a self-propelled flexible swimmer and address the role of the several components of the drag force in the scaling relations. Imposed deformations permit to isolate the hydrodynamic problem from the coupled fluid-structure problem present in swimming, but solved deformations are interesting to understand the true behavior of flexible swimmers. Tytell *et al.* [35] used a lattice Boltzman approach to consider the influence of body stiffness on the propulsion of a Lamprey-type 2D swimmer. Maneuvering has been considered by [36] using a 2D panel method similar to the one employed in this work to study swimmers undergoing maneuvers. This can be taken a step further by considering control algorithms to have the swimmer correct its behavior to achieve the desired course [37].

II. METHODOLOGY

A. Swimmer deformation and fluid problem

The swimmer is modeled by a 2D flexible but nonextensible curve representing its spine as shown in Fig. 1(a). An imposed traveling wave of deformation is imposed along the swimmer's length. The lateral displacement relative to the center of mass is of the form

$$y(s,t) = \frac{0.5A(\frac{s}{L}+\epsilon)}{1+\epsilon}\sin\left(\frac{2\pi}{\lambda}s-\omega t\right), \tag{2}$$

where λ is the wavelength, L is the body length, A is the tail beat amplitude taken from minimum to maximum transverse displacement, t is the time, ω is the angular frequency, s is the curvilinear position along the swimmer with $s=0$ at the head, and $s=L$ taken to be the tail. The constant ϵ alters the proportion of the tail amplitude exhibited by the head. ϵ and λ/L are set to 0.25 and 1, respectively, as typical values [30]. The center of mass is situated at $s=L/2$. The influence of the location of this center of mass does not drastically change the swimming gaits [21].

A 2D, unsteady panel method with a vortex particle representation of the wake [38,39] is implemented to numerically solve the fluid problem and account for the Kutta condition at the trailing edge of the swimmer ($s=L$). We approximate the swimmer boundaries with 20 flat, constant strength, dipole panels whose end nodes are placed along the spinal curve [34]. The Kutta condition is enforced by shedding a point vortex at each time step. The swimmer is immersed in idealized water of density $\rho = 1000\,\mathrm{kg\,m^{-3}}$. The fluid is inviscid and no parasitic drags, skin friction nor pressure drag, are initially present.

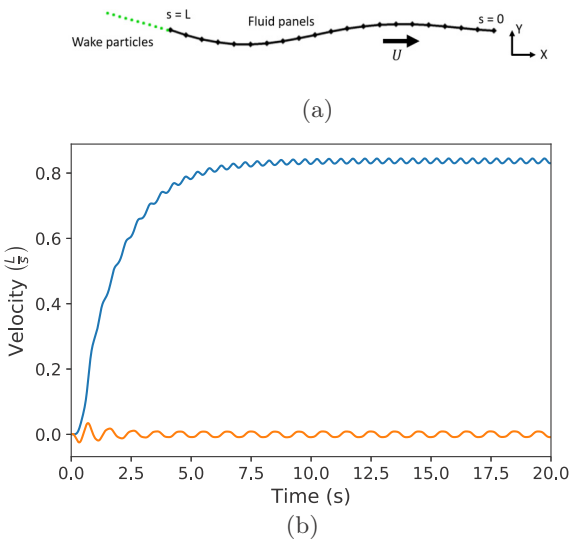

FIG. 1. (a) The swimmer is modeled by a inextensible, flexible, thin curve which is discretized into fluid panels with its wake represented by point vortices. (b) Typical temporal evolution of the horizontal (blue) and vertical (orange) velocity components of the center of mass, obtained for the parameters $M = 100$ kg m^{-1}, $L = 1$ m, $C_p = 0.01$, $A^\star = 0.2$, and $\omega = 2\pi$ rad s^{-1}.

Finally, the system moves following the second law of Newton and the velocity $\vec{U}$ of the center of mass is given by

$$M d\vec{U}(t)/dt = \vec{F}_H(t) + \vec{F}_D(t), \tag{3}$$

where M is the mass per unit span of the swimmer, $\vec{F}_H$ is the force per unit span calculated by the solver due to the fluid-structure interaction, and $\vec{F}_D$ is the contribution of the parasitic drag (Sec. II B). This introduces another dimensionless quantity, the dimensionless mass $M/\rho L^2$. We have checked that this quantity does not modify the steady-state swimming velocity U as long as $M/\rho L^2 \ll 1$, as already observed for rigid swimmers [21], but impacts the time of the transient regime. Note that $\vec{F}_H$ accounts for the fluid-swimmer interaction as a whole. We expect this force to have both positive components that contribute to the total thrust with the scaling $\rho L A^2 f^2$ per unit span as well as negative components that contribute to the drag, the so-called vortex-induced drag. Simulations stop when the steady state is reached. In the small-amplitude limit and in the turbulent regime characterized by a pressure drag coefficient C_P (Sec. II B), the transient time scales as $\frac{M}{\omega\rho LA\sqrt{C_P}}$ as shown with a simple model of self-propulsion [21]. We remark here that this 2D approximation omits finite-size effects, that might be important in 3D flows, like described in [40,41]

In practice, all simulations are stopped once the swimming velocity stabilizes to its steady-state value. Typically, simulations were run between 100 and 500 oscillation periods for large and small amplitudes, respectively. Multiplying the simulation duration by 10 did not alter the results; we estimate the error below 1%. In Fig. 1(b), we show the typical transient of the locomotion velocity, before converging towards its steady regime. For large time, $U(t)$ reaches a constant value, modulated by a periodic signal, with a frequency doubled with respect to the driving deformation [21].

In Secs. III A and III B, we take $M = 100$ kg m^{-1} and $L = 1$ m. In Sec. III C, simulations were performed with $M = 0.08$ kg m^{-1} and $L = 0.08$ m. These choices are subjective but not restrictive since results will be given in terms of dimensionless quantities.

B. Parasitic drag force

The aforementioned model is purely inviscid and does not account for any parasitic drag. This force per unit span is added in Newton's laws with two contributions, skin friction and pressure drags:

$$F_D(t) = \frac{1}{2}\rho(2L)U(t)^2(C_P + C_F), \tag{4}$$

where $U(t)$ is the instantaneous velocity of the swimmer's mass center, $C_F = \frac{4}{3}\frac{\alpha}{\sqrt{\mathrm{Re}(t)}}$ measures the skin friction coefficient with $\alpha = 1$ the value for a Blasius flat plate, and C_P the pressure drag coefficient. We have used two well-established expressions for the parasitic drag valid for motionless bodies. Both of them are weighted by dimensionless coefficients, respectively α and C_P, that can be systematically and easily varied all along the study. On the other hand, the vortex-induced drag is associated to the deformation of the swimmer and quantifies the difference with respect to a motionless body. This component of the total drag is directly measured from the calculation of the flow and will be characterized in what follows.

The two terms introduced in the parasitic drag need clarifications. First, as stated in the Introduction, values of the pressure drag coefficient C_P are below unity. In the turbulent regime we will consider values between 0 and 0.1. Second, $\alpha > 1$ will be used to represent the drag amplification of Bone-Lighthill boundary layer thinning in the skin friction term, which originates from finite-size effects [27–29]. In these references, the authors show that α should be proportional to the square root of the ratio of the transverse and longitudinal velocities, and we consequently varied α between the values 1 and 16, to account for this effect on the boundary layer and cover the values proposed in the aforementioned references.

Finally, the two terms have the same weight if $\mathrm{Re} \sim (4\alpha/3C_P)^2$. With typical values $\alpha \sim 1$ and $C_P \sim 0.01$, a transition occurs around $\mathrm{Re} \sim 10^4$ between a skin friction dominated drag and a pressure dominated drag. This value seems consistent with the value 3000 observed for natural swimmers [12] but actually it depends a lot on the exact values of α and C_P. In fact, we will see that $\alpha \sim 4$ for natural swimmer in the framework of our approach and that the value of the drag force does not vary much with C_P in the turbulent regime as long as the vortex-induced drag is accounted for. In what follows, we will set $C_P = 0$ to study the laminar regime ($\mathrm{Re} \lesssim 10^3$–$10^4$) and $C_F = \alpha = 0$ to study the turbulent regime ($\mathrm{Re} \gtrsim 10^3$–10^4).

III. RESULTS

A. Vortex-induced drag

First, we study the case $C_F = C_P = 0$ as a reference. Although the parasitic drag equals zero, the total drag is nonzero due to the oscillation of the hydrofoil. From a simple scaling analysis, we expect St to be a function of $A^\star$ only since the other dimensionless quantities ϵ and λ/L are fixed. To check the consistency of the simulations we vary both $A^\star$ in the range [0–0.3] and the Swimming number in the range [10^2–10^8] that covers both the laminar and turbulent flow regimes. First, we plot St as a function of Sw in Fig. 2(a). As expected, St is independent of Sw and is a function of $A^\star$ only. The relation between St and $A^\star$ is displayed in Fig. 2(b) where we see that all the data collapse on a single curve. St seems proportional to $A^\star$ at the leading-order approximation, but one higher term is needed at least to account for the trend.

As described in the Introduction, the vortex-induced drag force exhibits two contributions in the small-amplitude regime: the first one is similar to those of a stationary hydrofoil in a steady flow (the so-called lift-induced drag) which scales as $\rho U^2A^2/L$, while the second one appears through unsteady motions which in turn behaves as ρUA^2f. With a thrust per unit span scaling as ρLA^2f^2, the horizontal momentum balance leads to a relation between St and $A^\star$:

$$\mathrm{St}^2 = k_2(A^\star)^2 + k_1\mathrm{St}A^\star, \tag{5}$$

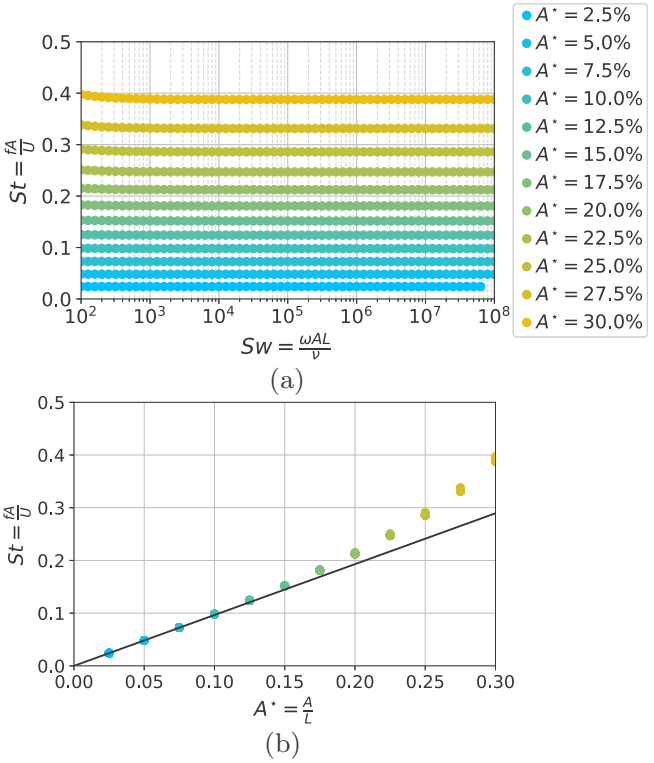

FIG. 2. Strouhal number without any parasitic drag. (a) St as a function of Sw. (b) St as a function of $A^\star = A/L$. The solid line is the linear interpolation in the small-amplitude regime ($A^\star < 0.1$). All the data from the (a) have been represented here.

with k_2 and k_1 two numerical factors. This simple balance predicts that for unimportant parasitic drag the Strouhal number is proportional to the ratio $A^\star$:

$$\mathrm{St} = pA^\star \text{ with } p = \frac{k_1}{2}\left(1 + \sqrt{1 + 4\frac{k_2}{k_1^2}}\right) \tag{6}$$

a proportionality constant. Analysis of data provided by simulations of rigid hydrofoils [42,43] suggests that this proportionality relation could hold whatever the geometry of the swimmer in the small-amplitude regime with a proportionality constant around unity. In our geometry, it is evaluated in the small-$A^\star$ limit ($A^\star < 0.1$) from Fig. 2 and $p = 0.965 \pm 0.004$. From Eq. (6), $k_1 = p - k_2/p$ and we take $k_1 = 0.965 - k_2/0.965$ in what follows. We will discuss the moderate $A^\star$ regime in the next section.

B. Pressure drag and turbulent regime

If we add a pressure drag characterized by a constant drag coefficient C_P, we expect now St to be a function of both $A^\star$ and C_P. The variations of the Strouhal number are represented in Fig. 3 with C_P varying between 0 and 0.1 and $A^\star$ varying between 0 and 0.3. In the limit $A^\star \to 0$, the contribution of the vortex-induced drag should be negligible and we expect the thrust per unit span scaling as $\rho L A^2 f^2$ to be balanced by the pressure drag per unit span scaling as $\rho C_P L U^2$, or simply $\mathrm{St}^2 \propto C_P$. In the general case, if we assume that we can simply add the contributions of the pressure

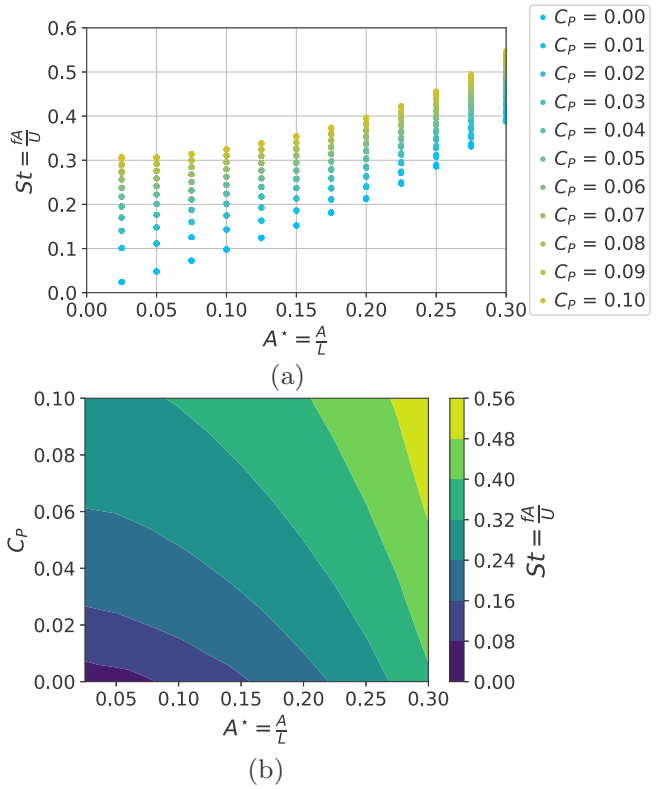

FIG. 3. (a) Strouhal number St as a function of $A^\star = A/L$ for several values of C_P. (b) Color plot representing St as a function of both $A^\star = A/L$ and C_P.

and vortex-induced drags, we should expect

$$\mathrm{St}^2 = k_2(A^\star)^2 + k_1 \mathrm{St} A^\star + k_0 C_P + g(A^\star, \mathrm{St}), \tag{7}$$

where $g(A^\star, \mathrm{St})$ is the function that accounts for large-amplitude effects in the vortex-induced drag. The coefficients k_0, k_1, and k_2 are inferred by restricting our analysis to the small-amplitude regime: given $k_1 = p - k_2/p$, we can reorganize the equation in

$$p\frac{\mathrm{St}}{A^\star} = -k_2 + k_0 \frac{pC_P}{A^\star(\mathrm{St} - pA^\star)}. \tag{8}$$

In Fig. 4(a), $p\frac{\mathrm{St}}{A^\star}$ is plotted as a function of $\frac{pC_P}{A^\star(\mathrm{St}-pA^\star)}$. In the limit $A^\star < 0.1$, there is a very good linear relation that is fitted with $k_0 = 0.910 \pm 0.004$ and $k_2 = 0.729 \pm 0.002$, and $k_1 = 0.210 \pm 0.002$ consequently. For larger $A^\star$ we observe a deviation from the linear trend that emphasizes the role of $g(A^\star, \mathrm{St})$, which is estimated from the relation (7). In Fig. 4(b), g/St^2 is plotted as a function of $A^\star$ to evaluate the relative contribution of the large-amplitude effects. As expected, there is a main trend but no perfect collapse since $g(A^\star, \mathrm{St})$ is expected to depend on both $A^\star$ and St, two quantities that can not be dissociated.

Here, important remarks come into sight when dealing with the turbulent regime. We first notice that for $A^\star \sim 0.2$, i.e., the value measured on natural fish in the turbulent regime, the Strouhal number is found between 0.2 and 0.4 whatever C_P between 0 and 0.1. This range matches exactly to that observed for natural swimmer: the combination of both the pressure and vortex-induced drags gives a Strouhal number insensitive to the drag coefficient. This is rationalized by the fact that the

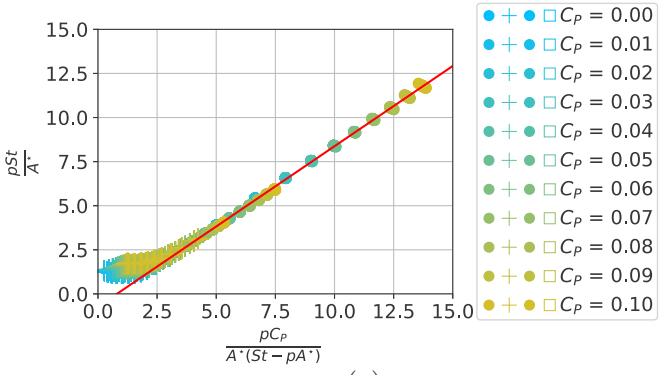

(a)

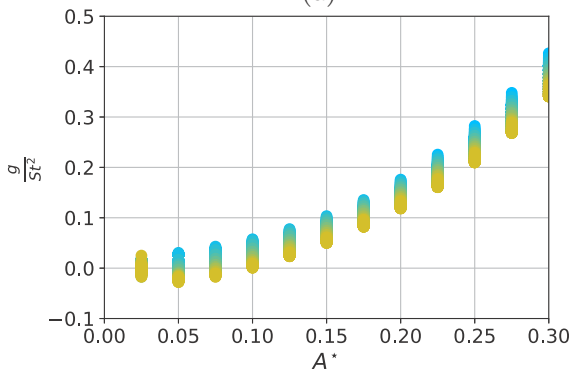

(b)

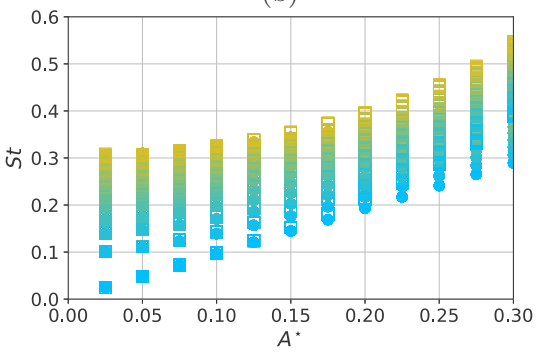

(c)

FIG. 4. (a) $p\frac{St}{A^\star}$ as a function of $\frac{pC_P}{A^\star(St-pA^\star)}$. The linear interpolation is performed on the data with $A^\star < 0.1$. The disk symbols represent the numerical points with $A^\star < 0.1$, while the crosses $A^\star \geqslant 0.1$. (b) g/St^2 as a function of $A^\star$ for all the data. (c) St as a function of $A^\star$ for all the data [open squares, as reported from Fig. 3(a)] and its comparison with the small-amplitude limit using disks, predicted by Eq. (9).

term $\rho U^2 A^2/L$ dominates the vortex-induced drag per unit span. Since the ratio $A^\star \sim 0.2$ is fixed for most fish, this contribution scales as $\rho L U^2$ as does the pressure drag. The relative contribution of the pressure and vortex-induced drags, respectively, depends on the exact value of C_P but does not lead to significant variations of St in the range of C_P characterizing fish.

Concerning the contribution of the large-amplitude effects, it reaches around 15% whatever C_P, as $A^\star \simeq 0.2$. We can deduce that most of the total drag force is accounted for by small-amplitude effects. We evaluate the three contributions by taking $A^\star = 0.2$ and $St = 0.3$; in that case $k_1 A^\star St \sim$

0.013 and $k_2(A^\star)^2 \sim 0.029$. Hence, the pressure drag term $k_0 C_P$ becomes dominant for $C_P \sim 0.046$. Solving the equation (8), we get

$$\mathrm{St} = \frac{A^\star(p^2 - k_2) + \sqrt{(A^\star)^2(k_2 + p^2)^2 + 4k_0 p^2 C_p}}{2p}. \tag{9}$$

We remark here that as $A^\star$ becomes high enough, the pressure drag is not dominant anymore, and we deduce that the Strouhal number becomes proportional to $A^\star$ following Eq. (6). The comparison of the small-amplitude regime given by Eq. (9) and the data of the simulation is plotted in Fig. 4(c).

As a last comment, we recall that ϵ and λ/L were not varied systematically but we do not expect significant effects. Leading-edge suction is not captured in our approach, nevertheless, it might play a significant role in the thrust for some fishes [44]. This could modify the value of the coefficients to some extent and this contribution could be implemented in our model as a future improvement. 3D effects are also disregarded in our purely 2D approach and could modify the coefficient k_1 and k_2. Given the good agreement between the simulations and natural fish, we do not expect significant modifications. In addition, 3D flows could also require higher-order terms, for instance, proportional to A^4 as proposed by Raspa *et al.* [20], and modify the g function.

C. Skin friction drag and laminar regime

Now we set $C_P = 0$ and vary α to consider the influence of proportionally increasing the added Blasius flat plate drag from its unmodified value ($\alpha = 1$) to reach the drag amplification observed by [27–29] in the laminar regime. In order to estimate the effect of the coefficient α, $A^\star$ is first set to 0.025 and Sw varied systematically in the range $[10^1$–$10^4]$ by varying f. The resulting Re(Sw) curves are shown in Fig. 5(a). The exponents of the power law are consistent with the expected value $\frac{4}{3}$ whatever α. In a second study, the same simulations are performed with $A^\star = 0.2$ [Fig. 5(b)]. Actually, $\alpha \sim 4$ gives the best interpolation of the biological data reviewed by [12]. This value is significantly larger than that expected by the thinning of the Bone-Lighthill boundary layer, as described in [27–29]. In order to check our approach, we have also displayed in Fig. 5 the results obtained from direct numerical simulations (DNS) presented in [12], using both 2D and 3D swimmers. For 2D DNS, the best value for α is close to 3, while it increases to almost 5 in 3D DNS. Part of this difference can be rationalized with influence of some 3D geometrical effects than can not be accounted for by 2D approaches. It appears that the simple Blasius friction captures well the scaling for swimming. Hence, the rudimentary approach of coupling unsteady panel method with the skin friction seems to be very efficient to predict the swimming locomotion. In the moderate-amplitude case, we observe a slight deviation from the trends obtained in Fig. 5(a) and the exponent of the scaling law increases from 1.2 for $\alpha = 1$ to 1.34 for $\alpha = 16$. We conjecture these slope changes as the effect of the vortex-induced drag. For $\alpha = 16$ the skin friction seems to be the only dominant drag; as α is decreased, the vortex-induced drag modifies the force balance and decreases the exponent (we recall that an exponent 1 is expected if the vortex-induced drag becomes dominant). We exploit our balance approach to account for this feature. In the laminar regime, we expect the following expression to account for the skin friction:

$$\mathrm{St}^2 = k_2(A^\star)^2 + k_1 \mathrm{St} A^\star + k_3 \frac{4}{3} \frac{\alpha}{\sqrt{\mathrm{Re}}} + g(A^\star, \mathrm{St}), \tag{10}$$

where k_1 and k_2 are the constants introduced previously, and k_3 another numerical factor. In the small-amplitude regime, the nonlinear function $g(A^\star, \mathrm{St})$ is neglected and the Strouhal number writes

$$\mathrm{St} = \frac{1}{2} k_1 A^\star \left(1 + \sqrt{1 + 4\frac{k_2}{k_1^2} + \frac{16\alpha k_3}{3\sqrt{\mathrm{Re}} k_1^2 (A^\star)^2}}\right), \tag{11}$$

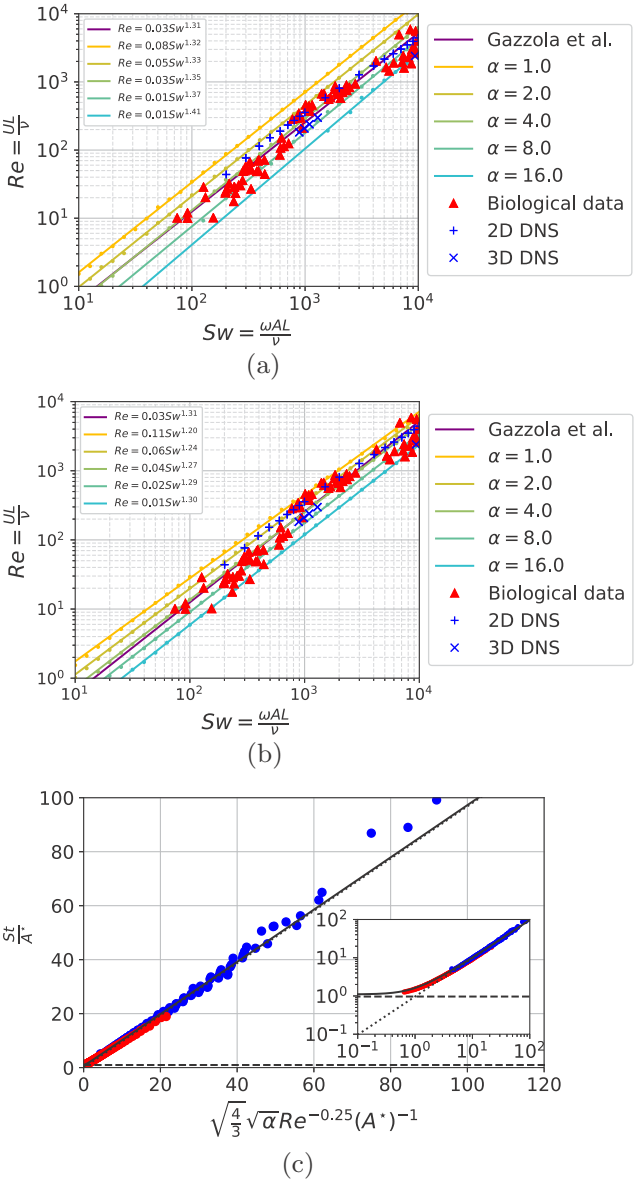

FIG. 5. (a) Re as a function of Sw. Data of the swimmer are given for several α between 1 and 16 and $A^\star = 0.025$. The biological data of the laminar regime and the interpolation by a power law [12] are represented as well. (b) Same figure but $A^\star = 0.2$ in simulation. For both figures, we have exhibited results from direct numerical simulations both in 2D and 3D geometries shown in [12], with $A^\star = 0.25$. (c) $\mathrm{St}/(A^\star)$ as a function of $\sqrt{\frac{4}{3}}\alpha^{1/2}\mathrm{Re}^{-1/4}(A^\star)^{-1}$ for all the data in (a) ($A^\star = 0.025$ in blue) and (b) ($A^\star = 0.2$ in red). The solid line is the model of Eq. (11) with $k_3 = 0.937$. The dotted line represents a proportionality law with a factor $\sqrt{k_3} = 0.968 \pm 0.002$. The dashed line represents $\mathrm{St}/(A^\star) = p = 0.965$. Inset: logarithmic scales.

which tends to the expression $\mathrm{St} = pA^\star$ [Eq. (6)] as Re tends to infinity. In the opposite limit where the skin friction dominates the drag, the Strouhal expression becomes

$$\mathrm{St} = 2\sqrt{k_3\frac{\alpha}{3}}\mathrm{Re}^{-1/4}. \tag{12}$$

Equation (11) is tested in Fig. 5(c) by plotting $\mathrm{St}/(A^\star)$ as a function of $\sqrt{\frac{4}{3}}\alpha^{1/2}\mathrm{Re}^{-1/4}(A^\star)^{-1}$ for all the data of Figs. 5(a) and 5(b). Everything collapses on a single master curve. The crossover between the two limit regimes occurs around $\sqrt{\frac{4}{3}}\alpha^{1/2}\mathrm{Re}^{-1/4}(A^\star)^{-1} \sim 1$ and the best fit of the data in the skin friction dominated regime leads to $k_3 = 0.937 \pm 0.004$.

By taking $A^\star = 0.2$ and $\mathrm{Re} = 3000$ (typical value at the onset of the turbulent regime), we find that the skin friction drag is always dominant in the laminar regime as long as $\alpha > 1.6$. This emphasizes why the scaling law introduced by [12] is robust. In addition, we can now give a more precise argument to discriminate between the laminar and turbulent regime and clarify the remark in Sec. II B. In the turbulent regime, we expect $\mathrm{St} \sim 0.3$. In the laminar regime $\mathrm{St} \sim 2.2\mathrm{Re}^{-1/4}$ with $\alpha \sim 4$. This leads to a transition around 3000 as observed in nature [12].

IV. CONCLUSIONS

In this article, we have exploited numerical simulations to question the influence of various drags at play in the force balance of an undulating swimmer. By varying the dimensionless tail beat amplitude $A^\star$ and the Swimming number, we have studied the impact of the pressure drag, the skin friction, and the vortex-induced drag. In the laminar regime, typically $\mathrm{Re} \lessapprox 3000$, we show that the vortex-induced drag might be neglected as long as the magnitude of the skin friction is large enough, i.e., $\alpha > 1.6$, which is the case for natural swimmer with a value for α around 4. This estimate is at least twice as large as the prediction proposed by Ehrenstein and Eloy in [27,28] and shows that our 2D swimmer needs to account for a significant amplification of the drag force to match the biological data. In the turbulent regime, typically $\mathrm{Re} \gtrapprox 3000$, we show that the combination of both the pressure and vortex-induced drags sets the Strouhal number between 0.2 and 0.4 following the thrust and drag balance, in very good agreement with natural swimmers.

ACKNOWLEDGMENTS

The authors acknowledge project funding by the UCA$^{\mathrm{JEDI}}$ IDEX grant (ANR-15-IDEX-01), and the support from MyCFD. J. Sánchez-Rodríguez is thanked for enlightening discussions.

[1] M. Sfakiotakis, D. M. Lane, and J. B. C. Davies, Review of fish swimming modes for aquatic locomotion, IEEE J. Oceanic Eng. **24**, 237 (1999).
[2] R. Bainbridge, The speed of swimming of fish as related to size and to the frequency and amplitude of the tail beat, J. Exp. Biol. **35**, 109 (1958).
[3] R. Bainbridge, Speed and stamina in three fish, J. Exp. Biol. **37**, 129 (1960).
[4] P. Webb, P. Kostecki, and E. Stevens, The effect of size and swimming speed on locomotor kinematics of rainbow trout, J. Exp. Biol. **109**, 77 (1984).
[5] P. W. Webb, The swimming energetics of trout, J. Exp. Biol. **55**, 489 (1971).
[6] M. S. Triantafyllou, G. S. Triantafyllou, and R. Gopalkrishnan, Wake mechanics for thrust generation in oscillating foils, Phys. Fluids A **3**, 2835 (1991).
[7] G. S. Triantafyllou, M. S. Triantafyllou, and M. A. Grosenbaugh, Optimal thrust development in oscillating foils with application to fish propulsion, J. Fluids Struct. **7**, 205 (1993).
[8] M. S. Triantafyllou, F. S. Hover, A. H. Techet, and D. K. Yue, Review of hydrodynamic scaling laws in aquatic locomotion and fishlike swimming, Appl. Mech. Rev. **58**, 226 (2005).

[9] E. Tytell, The hydrodynamics of eel swimming ii. effect of swimming speed, J. Exp. Biol. **207**, 3265 (2004).
[10] C. Eloy, Optimal Strouhal number for swimming animals, J. Fluids Struct. **30**, 205 (2012).
[11] G. K. Taylor, R. L. Nudds, and A. L. Thomas, Flying and swimming animals cruise at a Strouhal number tuned for high power efficiency, Nature (London) **425**, 707 (2003).
[12] M. Gazzola, M. Argentina, and L. Mahadevan, Scaling macroscopic aquatic locomotion, Nat. Phys. **10**, 758 (2014).
[13] M. Saadat, F. E. Fish, A. G. Domel, V. Di Santo, G. V. Lauder, and H. Haj-Hariri, On the rules for aquatic locomotion, Phys. Rev. Fluids **2**, 083102 (2017).
[14] D. Floryan, T. Van Buren, and A. J. Smits, Efficient cruising for swimming and flying animals is dictated by fluid drag, Proc. Natl. Acad. Sci. U.S.A. **115**, 8116 (2018).
[15] I. E. Garrick, Propulsion of a flapping and oscillation aerofoil: NACA Technical Report No. 567, Washington: NACA, 1936 (unpublished).
[16] T. Y. Wu, Hydromechanics of swimming propulsion. part 3. swimming and optimum movements of slender fish with side fins, J. Fluid Mech. **46**, 545 (1971).
[17] D. B. Quinn, G. V. Lauder, and A. J. Smits, Scaling the propulsive performance of heaving flexible panels, J. Fluid Mech. **738**, 250 (2014).
[18] D. Floryan, T. Van Buren, C. W. Rowley, and A. J. Smits, Scaling the propulsive performance of heaving and pitching foils, J. Fluid Mech. **822**, 386 (2017).
[19] F. Gibouin, C. Raufaste, Y. Bouret, and M. Argentina, Study of the thrust–drag balance with a swimming robotic fish, Phys. Fluids **30**, 091901 (2018).
[20] V. Raspa, S. Ramananarivo, B. Thiria, and R. Godoy-Diana, Vortex-induced drag and the role of aspect ratio in undulatory swimmers, Phys. Fluids **26**, 041701 (2014).
[21] J. Sánchez-Rodríguez, C. Raufaste, and M. Argentina, A minimal model of self propelled locomotion, J. Fluids Struct. **97**, 103071 (2020).
[22] M. Lighthill, Large-amplitude elongated-body theory of fish locomotion, Proc. R. Soc. London B **179**, 125 (1971).
[23] J. Videler, Swimming movements, body structure and propulsion in cod gadus morhua, Symp. Zool. Soc. London **48**, 1 (1981).
[24] T. Tandler, E. Gellman, D. De La Cruz, and D. J. Ellerby, Drag coefficient estimates from coasting bluegill sunfish lepomis macrochirus, J. Fish Biol. **94**, 532 (2019).
[25] T. G. Lang, Speed, power, and drag measurements of dolphins and porpoises, in *Swimming and Flying in Nature*, Vol. 2, edited by T. Y.-T. Wu, C. J. Brokaw, and C. Brennen (Springer, Boston, MA, 1975), pp. 553–572.
[26] J. Videler and P. Kamermans, Differences between upstroke and downstroke in swimming dolphins, J. Exp. Biol. **119**, 265 (1985).
[27] U. Ehrenstein and C. Eloy, Skin friction enhancement in a model problem of undulatory swimming, in *11th International Conference of Numerical Analysis and Applied Mathematics 2013*, *AIP Conference Proceedings, Vol.* 1558 (AIP, Melville, NY, 2013), p. 273.
[28] U. Ehrenstein and C. Eloy, Skin friction on a moving wall and its implications for swimming animals, J. Fluid Mech. **718**, 321 (2013).
[29] U. Ehrenstein, M. Marquillie, and C. Eloy, Skin friction on a flapping plate in uniform flow, Philos. Trans., Ser. A **372**, 1 (2014).
[30] J. Carling, T. L. Williams, and G. Bowtell, Self-propelled anguilliform swimming: simultaneous solution of the two-dimensional navier-stokes equations and Newton's laws of motion, J. Exp. Biol. **201**, 3143 (1998).
[31] A. Leroyer and M. Visonneau, Numerical methods for ranse simulations of a self-propelled fish-like body, J. Fluids Struct. **20**, 975 (2005).
[32] M. Gazzola, P. Chatelain, W. M. Van Rees, and P. Koumoutsakos, Simulations of single and multiple swimmers with non-divergence free deforming geometries, J. Comput. Phys. **230**, 7093 (2011).
[33] T. Pedley and S. Hill, Large-amplitude undulatory fish swimming: fluid mechanics coupled to internal mechanics, J. Exp. Biol. **202**, 3431 (1999).

[34] D. Gross, Y. Roux, and M. Argentina, Curvature-based, time delayed feedback as a means for self-propelled swimming, J. Fluids Struct. **86**, 124 (2019).
[35] E. D. Tytell, C.-Y. Hsu, T. L. Williams, A. H. Cohen, and L. J. Fauci, Interactions between internal forces, body stiffness, and fluid environment in a neuromechanical model of lamprey swimming, Proc. Natl. Acad. Sci. U.S.A. **107**, 19832 (2010).
[36] K. Singh, Hydrodynamics of flexible manoeuvres in fish, Ph.D. thesis, University of Cambridge, 2009 .
[37] J. B. Melli, A hierarchy of models for the control of fish-like locomotion, Ph.D. thesis, Princeton University, 2008 .
[38] C. Rehbach, Calcul d'écoulements autour d'ailes sans epaisseur avec nappes tourbillonnaires evolutives, Recherche Aérospatiale **2**, 53 (1973).
[39] C. Rehbach, Numerical calculation of three-dimensional unsteady flows with vortex sheets, in *16th Aerospace Sciences Meeting* (AIAA, Reston, VA, 1978), p. 111.
[40] F. Ayancik, Q. Zhong, D. B. Quinn, A. Brandes, H. Bart-Smith, and K. W. Moored, Scaling laws for the propulsive performance of three-dimensional pitching propulsors, J. Fluid Mech. **871**, 1117 (2019).
[41] U. Ehrenstein, Thrust and drag scaling of a rigid low-aspect-ratio pitching plate, J. Fluids Struct. **87**, 39 (2019).
[42] K. W. Moored and D. B. Quinn, Inviscid scaling laws of a self-propelled pitching airfoil, AIAA J. **57**, 3686 (2019).
[43] J. Labasse, U. Ehrenstein, and P. Meliga, Numerical exploration of the pitching plate parameter space with application to thrust scaling, Appl. Ocean Res. **101**, 102278 (2020).
[44] K. N. Lucas, G. V. Lauder, and E. D. Tytell, Airfoil-like mechanics generate thrust on the anterior body of swimming fishes, Proc. Natl. Acad. Sci. U.S.A. **117**, 10585 (2020).